Annealing-induced bi bilayer on Bi_2Te_3 investigated via quasi-particle-interference mapping

Annealing-Induced Bi Bilayer on Bi_2Te_3 Investigated *Via* Quasi-Particle-Interference Mapping

Koen Schouteden[a]*, Kirsten Govaerts[b], Jolien Debehets[c], Umamahesh Thupakula[a], Taishi Chen[d], Zhe Li[a], Asteriona Netsou[a], Fengqi Song[e], Dirk Lamoen[b], Chris Van Haesendonck[a], Bart Partoens[b], and Kyungwha Park[f]

a) Solid-State Physics and Magnetism Section, KU Leuven, BE-3001 Leuven, Belgium

b) EMAT and CMT group, Department of Physics, Universiteit Antwerpen, B-2020 Antwerpen, Belgium

c) Department of Materials Engineering, KU Leuven, BE-3001 Leuven, Belgium

d) Max Planck Institute for Chemical Physics of Solids, Dresden, Germany

e) National Laboratory of Solid State Microstructures, Collaborative Innovation Center of Advanced Microstructures, and Department of Physics, Nanjing University, Nanjing 210093, China

f) Department of Physics, Virginia Tech, Blacksburg, Virginia 24061, USA

* koen.schouteden@fys.kuleuven.be

ABSTRACT Topological insulators (TIs) are renowned for their exotic topological surface states (TSS) that reside in the top atomic layers and hence detailed knowledge of the surface top atomic layers is of utmost importance. Here we present the remarkable morphology changes of Bi_2Te_3 surfaces, which are freshly cleaved in air, upon subsequent systematic annealing in ultra-high vacuum and the resulting effects on the local and area-averaging electronic properties of the surface states, which are investigated by combining scanning tunneling microscopy (STM), scanning tunneling spectroscopy (STS), and Auger electron spectroscopy (AES) experiments with density functional theory (DFT) calculations. Our findings demonstrate that the annealing induces the formation of a Bi bilayer atop the Bi_2Te_3 surface. The adlayer results in *n*-type doping and the atomic defects act as scattering centers of the TSS electrons. We investigated the annealing-induced Bi bilayer surface on Bi_2Te_3 also *via* voltage-dependent quasi-particle-interference (QPI) mapping of the surface local

density of states and *via* comparison with the calculated constant-energy contours and QPI patterns. We observed *closed* hexagonal patterns in the Fourier transform of real-space QPI maps with secondary outer spikes. DFT calculations attribute these complex QPI patterns to the appearance of a "second" cone due to the surface charge transfer between the Bi bilayer and the Bi_2Te_3. Annealing in ultra-high vacuum offers a facile route for tuning of the topological properties and may yield similar results for other topological materials.

KEYWORDS Topological insulators, Bi_2Te_3, Bi bilayer, scanning tunneling microscopy, quasi-particle interference, density functional theory.

Topological insulators (TIs) have much potential for use in practical applications because of their unique electronic properties, which are mainly related to two-dimensional (2D) topological surface states (TSS) exhibiting Dirac dispersion. Bi_2Te_3, Bi_2Se_3, and Sb_2Te_3 are TIs that have drawn lots of attention due to a single topological surface-state Dirac cone.[1] They have a layered structure in units of quintuple layers (QLs) along the crystal *c*-axis, where one QL consists of B-A-B-A-B stacking for the TIs A_2B_3. The coupling between the adjacent QLs is dominated by van der Waals interactions, similar to graphite. The van der Waals gap between the QLs yields a preferential cleavage between the adjacent Te or Se layers,[2] yet cleavage within a QL rather than between two successive QLs may also occur.[3-5] Moreover, TI surfaces appear to be affected by spontaneous reorganization after the cleavage.

Since the TSS of TIs resides within the topmost atomic layers of the TI surface, its precise characteristics depends on surface structure and composition. Hence detailed knowledge of the surface top atomic layers is of utmost importance. Recently, Bi_2Te_3 samples where the surface was obtained from ion sputtering and subsequent annealing revealed coexistence of QL-termination and Bi-bilayer termination.[5] Similarly, it was reported that Bi_2Se_3 samples cleaved in ultra-high vacuum (UHV)

spontaneously form a Bi bilayer on the topmost QL at room temperature.[6] Furthermore, Bi accumulation may occur at the Bi_2Se_3 surface *via* diffusion of Bi[7] that can be intercalated in between the QLs.[8,9] In contrast, Hewitt *et al*.[10] reported that Bi_2Se_3 crystals cleaved in UHV predominantly show the Se surface termination, while those stored in air for a long time have a high probability for Bi termination. Despite these previous investigations, it is not yet clear how the morphology and composition of the TI surface is modified upon exposure to elevated temperatures without applying ion bombardment as in Ref. [5], which can be very invasive for the surface. Moreover, there is a lack of studies of *local* electronic properties of a Bi-bilayer terminated Bi_2Te_3 surface, especially quasi-particle interference (QPI) near surface scatterers. The reported local properties of a Bi bilayer surface on Bi_2Se_3 [11] cannot be directly applied to the Bi_2Te_3 case because different surface-state and bulk band structures of Bi_2Te_3 and Bi_2Se_3 influence the Bi bilayer surface differently.

Here we present the remarkable morphology changes of freshly cleaved Bi_2Te_3 surfaces upon systematic annealing in UHV and the resulting effects on the local and area-averaging electronic properties of the surface states, by applying scanning tunneling microscopy/spectroscopy (STM/STS) and Auger electron spectroscopy (AES) combined with density functional theory (DFT) calculations. Our findings demonstrate that without an intentional Bi bilayer adsorption or invasive ion bombardment, the annealing itself induces the formation of a Bi bilayer atop the Bi_2Te_3 surface. We investigated the annealing-induced Bi bilayer surface on Bi_2Te_3 *via* QPI mapping of the surface local density of states (LDOS) and *via* comparison with the calculated QPI patterns. The Fourier transform (FT) of our observed real-space QPI mapping exhibits a completely closed hexagonal shape with layers of secondary outer peaks below 150 mV, which is distinct from QPI patterns for a Te-terminated Bi_2Te_3 surface in Refs. [12-14]. Our experimental data are supported by our calculated QPI patterns for the Bi-bilayer terminated Bi_2Te_3 based on DFT.

Results

In our experiments, the Bi_2Te_3 sample is exfoliated with an adhesive tape in ambient conditions and installed within a few minutes in the introduction chamber of the UHV STM setup. Prior to annealing in UHV, very large flat terraces are retrieved with a lateral size of 10 µm or larger (Fig. 1a). The terraces exhibit a sub-monolayer amount of nanosized species and holes (Fig. 1c) attributed to exfoliation-related damage of the top QL and to contamination due to brief exposure to ambient conditions (*e.g.*, H_2O, O_2 and N_2). Steps in between two terraces typically have a height of 0.95 ± 0.05 nm, *i.e.*, the height of a full QL,[3] or multiples of that.

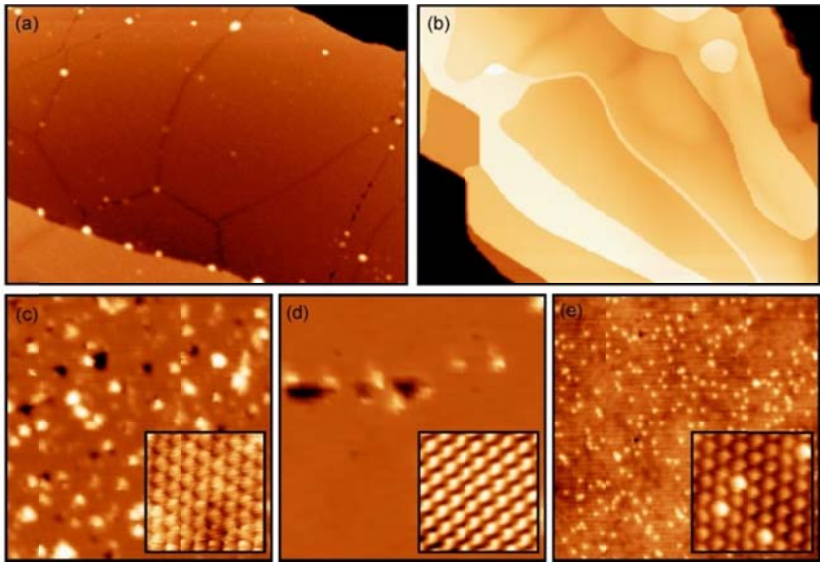

Figure 1: Modification of the sample topography by annealing. Typical large-scale STM topographies of (a) the freshly cleaved Bi_2Te_3 surface prior to annealing (1500 x 1500 nm^2; setpoint values V = +1.0 V and I = 0.05 nA) and (b) after annealing to 420 °C (500 x 350 nm^2; setpoint values V = +0.8 V and I = 0.2 nA). (c)-(e) 40 x 40 nm^2 close-up view STM topographies of the Bi_2Te_3 surface (c) prior to annealing and after annealing to (d) 200 °C and (e) 420 °C, respectively. Setpoint values are (c) V = +1.0 V and I = 0.05 nA, (d) V = +1.0 V and I = 0.03 nA, and (e) V = +0.2 V and I = 0.5 nA (T_{sample} = 4.5 K). Color height scales of (c), (d), and (e) are 0.6

nm, 0.3 nm, and 0.1 nm, respectively. Insets present 3 x 3 nm^2 atomically resolved close-up view of the corresponding surface.

Next, annealing in UHV conditions is applied to desorb surface contaminants. After annealing to 200 °C for about 2 hours (Fig. 1d), surface quality has improved considerably and locally atomically clean regions of about 20 x 20 nm^2 and larger can be retrieved, implying that surface restructuring has occurred. Remarkably, after annealing to 420 °C for about 24 hours (Fig. 1e), the surface shows atomically flat terraces that typically exhibit a minute amount of atomic-sized protrusions, referred to as "defects" hereafter, that have a random distribution. Height of these defect features is 0.05 ± 0.02 nm. Locally, regions without defects also exist. Measured in-plane atomic distances are 0.43 ± 0.01 nm, which agrees with reported values for the pristine Te-terminated (111) surface of Bi_2Te_3 in Refs. [12,15]. Defects are located exclusively at positions of the atomic lattice. Since a clean atomically flat surface was obtained after annealing to 200 °C, the observed defects must stem from the substrate and hence be either Bi or Te. Our annealing experiments indicate that the defect-type features start to appear after annealing to a temperature of 375 ± 10 °C.

More strikingly, after the annealing at 420 °C we find that the step heights are typically well below that of a full QL after the annealing, as illustrated in Figs. 2a and 2b. The higher-lying region on the left side of the step edge in Fig. 2a is defect-free and can be assigned to a full QL (QL #1) of the pristine Bi_2Te_3 that is stacked on top of another full QL (QL #2). As indicated above, in the experiments prior to annealing it is found that the height of a full QL with respect to the full QL below is 0.95 nm. Therefore in Fig. 2b, the height profile is given an offset so that the full QL #1 on the left hand side has a height level of 0.95 nm, *i.e.*, the height of a full QL (QL #1) stacked on top of another full QL (QL #2). The height of 0 nm hence corresponds to the top of QL #2. The lower-lying region on the right side of the step edge in Fig. 2a reveals a high density of defects. In the following we attribute the defect-rich regions to an annealing-induced adlayer that is (locally) covering the Bi_2Te_3 surface. The

step height measured in Fig. 2b is about 0.60 ± 0.05 nm as measured from the top of the full QL #1 on the left side, *i.e.*, the thickness of the adlayer on QL #2 is 0.35 ± 0.10 nm. The increased occurrence of sub-QL step heights indicates considerable surface restructuring and/or partial evaporation of the top QL at the annealing temperatures. More STM topographies of two other Bi_2Te_3 samples annealed at different temperatures also show similar features (Figs. SM-3 and SM-4). Te has a lower vapor pressure than Bi[16] and hence evaporation of Te is most likely to occur.

A step height histogram based on height profiles acquired on the entire sample is presented in Fig. 2e. The histogram in Fig. 2e reveals maxima around 0.37 ± 0.05 nm, 0.60 ± 0.05 nm and 0.95 ± 0.05 nm. For regions with a neighboring pristine surface, these step height values are consistent with interpretation in terms of an annealing induced Bi bilayer atop the pristine Bi_2Te_3 surface, as indicated in Fig. 2b and as will be discussed in full detail below. We note here that there also exist regions of the sample that do not have defect-free terraces (*i.e.*, defects exist on every terrace). For these regions no well-defined reference surface is available that can be used for interpretation of the sub-QL step height and hence the step height values cannot be unambiguously linked to a specific adlayer thickness or surface termination (see Fig. SM-5). In the following, we focus on regions that have a neighboring pristine Bi_2Te_3 terrace that allows us to identify these defect-rich regions as an adlayer with thickness of 0.35 ± 0.10 nm on top of a complete Bi_2Te_3 QL, similar to the region discussed in Fig. 2a.

In three series of experiments the same Bi_2Te_3 sample has been exposed to ambient, after which it was exfoliated in ambient and annealed under UHV conditions. As indicated above, after annealing to about 420 °C step heights well below a full QL are frequently observed. After exfoliating the same sample back under ambient conditions, again mainly step heights of a full QL are observed. This indicates that the applied annealing modifies the (top QLs of the) sample surface only and leaves the lower-lying QLs in the bulk of the sample unaltered.

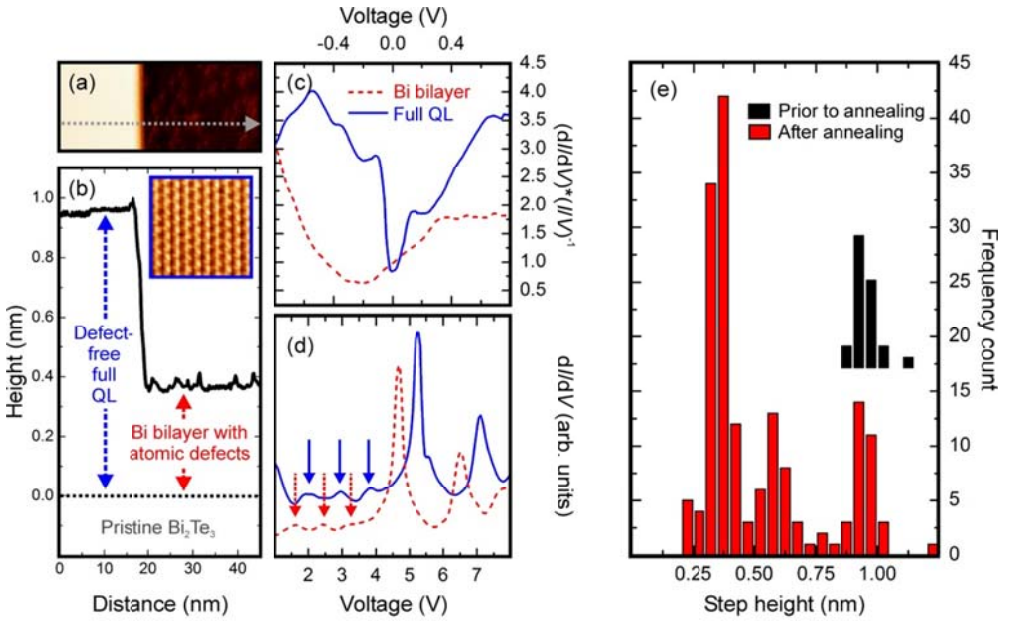

Figure 2: Doping effects on the Bi_2Te_3 surface by the adlayer after annealing at 420 °C. (a) 45 x 11 nm^2 STM topography of the Bi_2Te_3 surface comprising a step that separates a pristine defect-free region (left terrace) and an adlayer covered defect-rich region (right terrace) with about 200 defects per 1000 nm^2. (b) Height profile taken along the dotted line in (a). Inset shows an atomically resolved close-up view of the pristine region in (a). Orientation of the atomic lattice is the same for the adlayer region. (c) d*I*/d*V* spectra (open feedback loop) recorded on the two regions in (a). Setpoint values are 0.2 nA and -1.0 V. (d) d*I*/d*V* spectra (closed feedback loop) recorded on the two regions in (a). Setpoint values are 0.2 nA and +1.0 V. Curves are given an offset for clarity. Red and blue arrows indicate the energy positions of three weaker electronic resonances. T_{sample} = 4.5 K. (e) Frequency count of the step heights observed prior to annealing (black histogram) and after annealing to 420°C (red histogram). Prior to annealing, mainly steps with height of about 0.95 nm are observed and can be assigned to a full QL step. After annealing, mainly sub-QL steps are resolved.

In order to obtain insight into the characteristics of the sub-QL step height, we carried out complementary UHV AES experiments on two samples that were both freshly cleaved in ambient prior installation in UHV. One of the samples was annealed in a separate UHV chamber to 420°C and then

transported in a protective nitrogen environment to the AES setup. Figures 3a and 3b show the differentiated AES spectra of the two sample surfaces in the Bi and Te peak regions, respectively. The surface of the annealed sample exhibits a significantly higher Bi signal and a lower Te signal compared to that of the non-annealed sample, which implies a higher amount of Bi for the annealed sample. As the peak-to-peak height in the differentiated spectrum is directly proportional to the amount of that element present, this quantity can be used to compare the amount of that element at the surface of different samples. From Fig. 3, we infer a Te:Bi ratio of about unity for the non-annealed sample. This ratio remains the same after storage of the sample in UHV for one week (data not shown). In contrast, the annealed sample shows a Te:Bi ratio of about 0.5, *i.e.*, more Bi is present at the sample surface after annealing (our quantitative estimate of the ratios includes the uncertainties of about 20%[17]). We note that we do not know the precise AES probing depth for our samples (typically of the order of 1 nm, depending - among other things - on the surface roughness[43]). Nevertheless, these findings suggest that the applied annealing procedure gives rise to a higher Bi concentration close to the top surface, such as the formation of a Bi bilayer or a Bi_2-Te structure atop the Bi_2Te_3 surface. Below we will exclude the Bi_2-Te structure as a possibility. Bi(111) has an in-plane lattice constant which is similar to that of Bi_2Te_3, and so Bi(111) bilayers can adopt the same lattice constant as that of Bi_2Te_3, as illustrated in the inset of Fig.1e. Our observation is consistent with the recent report on the coexistence of small Bi(111) bilayer islands on top of Bi_2Te_3 after sputtering and annealing at 300 °C of the sample in UHV.[5]

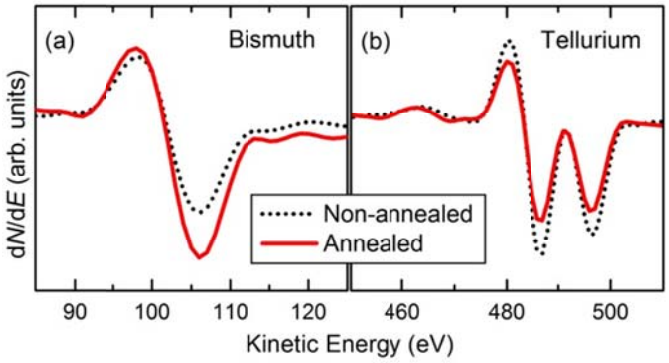

Figure 3: AES experiments. Differentiated AES spectra of a non-annealed and an annealed sample. (a) Bi energy region. (b) Te energy region.

Therefore, we interpret the defect-rich region in Fig. 2a as a Bi(111) bilayer on top of a full QL #2, while the defect-free region in Fig. 2a is interpreted as a full QL #1 without any cover layer. The thickness of the adlayer inferred from the height profile in Fig. 2b of around 0.35 ± 0.10 nm is consistent with previously reported values for Bi bilayers.[5] More evidences of the existence of a Bi bilayer on Bi_2Te_3 follow below.

Next, we probed the electronic structure of the pristine and the Bi bilayer regions in Fig. 2a by recording $(dI/dV)(V)$ spectra that reflect the surface LDOS, as illustrated in Figs. 2c and 2d. Clearly there exists a large difference between the two surfaces. The highest resonance of the pristine region in Fig. 2d occurs at about 5.3 eV, which matches a previously reported value of the vacuum level for pristine Bi_2Te_3 surfaces,[18] compared to about 4.7 eV for the bilayer region. This highest resonance shows only a minor dependence on the density of atomic defects (Fig. SM-8). The second resonance at higher voltages in Fig. 2d can be fully attributed to a so-called image-potential-state.[19] Upon careful inspection of Fig. 2d, one can resolve three additional characteristic resonances below the vacuum level, *i.e.*, around 2, 3 and 4 V (for the full QL region). These states can be assigned to higher-lying conduction bands of the Bi_2Te_3 surface, as we will demonstrate below using band structure calculations. Remarkably, all these resonances experience a downward shift to lower voltages on the

bilayer region, similar to the vacuum level related resonance. Similar observations are made at lower voltages near the Fermi level (Fig. 2c), where the local minimum in the (normalized) dI/dV spectra is shifted downward at the bilayer covered terrace. Corresponding non-normalized dI/dV spectra of the Bi_2Te_3 surface are presented in Fig. SM-1 and they are consistent with previously reported spectra in Ref. [20]. The observed downward shift of all electronic features can be explained by an *n*-type doping effect of the bilayer due to charge transfer from the Bi bilayer to the Bi_2Te_3, which gives rise to a lower work function and to a lowering of the surface electronic states of Bi_2Te_3 (*i.e.*, an increased binding energy).[8,21,22,23] Chen *et al*. reported a reduction of the work function by about 0.4 eV upon growing Bi bilayer islands with uniform height on Bi_2Te_3 using molecular beam epitaxy,[24] which is in good agreement with our observations.

To further confirm our interpretation of the surface adlayer as a Bi bilayer, we performed band structure calculations for different surface adlayer configurations and we determined the work functions of these configurations. The results are listed in the Table 1 below, together with their height with respect to the supporting Bi_2Te_3 substrate. The work function of the bare Bi_2Te_3 is in line with previous reports,[23] yet it should be kept in mind that the work function is typically underestimated in DFT-based calculations. From the considered configurations, Te+Bi+Te, Te+Bi_2, Bi_2+Te, and Te+Bi+Te+Bi_2 do not lead to a significant lowering of the work function compared to the bare Bi_2Te_3. Moreover, their height (thickness) is significantly higher than the adlayer height (thickness) observed in the experiments (Fig. 2b) and hence these configurations are ruled out as a possible adlayer. Based on their height and calculated work function, both a Bi bilayer and a Te+Bi layer remain a possibility. Considering Te desorption and/or diffusion of intercalated Bi towards the top surface during the annealing experiments, a Bi bilayer seems more favorable, and the corresponding downward shift of the calculated work function matches the experimental observations (Fig. 2d).

Table 1: Work function calculations. Work functions determined from band structure calculations for different surface adlayers, including a bare Bi_2Te_3 slab of 5 QLs as a reference.

Type	Bare (5QLs)	+Bi2 (opt)	+Te+Bi (opt)	Te+Bi+Te (unopt)	+Te+Bi2 (unopt)	Bi2+Te (unopt)	Te+Bi+Te+Bi2 (opt)
Height	0 nm	0.446 nm	0.420 nm	0.640 nm	0.595 nm	0.559 nm	1.027 nm
Work function	4.95 eV	4.64 eV	4.50 eV	5.08 eV	4.82 eV	4.89 eV	4.84 eV

Figure 4 presents the calculated density of states (DOS) of the bare Bi_2Te_3 surface and the Bi bilayer covered Bi_2Te_3 surface, based on band structure calculations (which will be discussed in detail later) of the respective systems. The calculated DOS results are in qualitative agreement with the experimental data in Fig. 2. In particular, the local minimum at the Fermi level in the top panel in Fig. 4 shifts to lower energies for the Bi bilayer covered surface, similar to Fig. 2c. At higher energies, the calculations in the bottom panel of Fig. 4 capture the existence of the higher-lying conduction bands of the Bi_2Te_3 surface[25] observed in Fig. 2d, as well as the shift of these resonances towards lower energies for the Bi bilayer covered surface. We note that the shape of the spectra in Fig. 4a differs from that in Fig. 2c. This may be at least partially accounted for by LDOS contributions of the STM tip apex to the experimental spectra, which is not considered in the calculations.

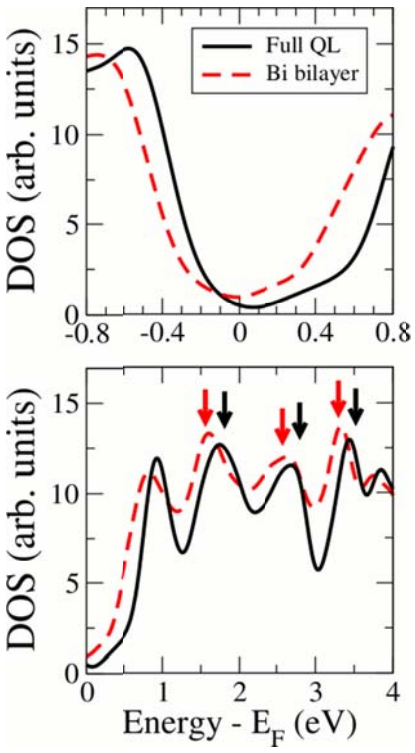

Figure 4: Calculated DOS. Total DOS calculated for the pristine QL-terminated 5 QLs (black solid curves) and for the Bi-bilayer adsorbed on 5 QLs (red dashed curves). To compare with the experimental data in Fig. 2, the DOS data is separated into two regions: a region near the Fermi level (top panel) and a higher-energy region (bottom panel).

Next, we investigated in detail the local electronic structure of the sample surface by using LDOS mapping referred to as a QPI mapping. Pristine regions remain featureless and reveal clear QPI patterns only near step edges (data not shown).[26] In contrast, bilayer regions reveal complex QPI patterns all across their terraces, as illustrated in the LDOS maps in Figs. 5b and 5c recorded on the bilayer region in Fig. 5a. To achieve clear QPI mapping, adatoms or surface dopants are often intentionally deposited and they become scattering centers of the surface electrons.[12,13] In our case, the atomic defects scatter the TSS electrons and create electron interference depending on the energy. Since the QPI maps exhibit a highly periodic character, they are better resolved in the FT image. Figures 5d-k present a series of voltage-dependent FT-QPI images recorded on the bilayer region in Fig. 5a. The FT-QPI images can be understood considering the allowed scattering wave vectors in the surface Brillouin zone. During

elastic scattering, an atomic defect scatters the incident wave with a wave vector $\boldsymbol{k}_i$ into $\boldsymbol{k}_f = \boldsymbol{k}_i + \boldsymbol{q}$, with $\boldsymbol{k}_i$ and $\boldsymbol{k}_f$ being on the same constant-energy contour (CEC), of which an example is shown in Fig. 6d. The quantum interference between the initial and final states results in a standing wave pattern whose spatial period is given by $2\pi/\boldsymbol{q}$. Our experimental FT-QPI patterns show much more features than the FT-QPI patterns reported for pristine Bi_2Te_3,[12,13,20,27] especially at voltages between -50 mV and +125 mV in Fig. 5. Typically, for scattering on pristine Bi_2Te_3 surfaces (except at very high voltages), the observed FT-QPI patterns show features only in the $\bar{\Gamma}$-$\bar{M}$ direction, *e.g.*, compare our data with Fig. 2 in Refs. [12, 20]. In the indicated voltage range however, we observe *closed* hexagonal patterns in the FT of real-space QPI including scattering peaks along the $\bar{\Gamma}$-$\bar{K}$ direction and secondary outer spikes. Some of these extra features along the $\bar{\Gamma}$-$\bar{K}$ direction are much more pronounced than those reported for pristine Bi_2Te_3 at much higher voltages (several 100 mV higher), *e.g.*, compare our data with Fig. 2f in Ref. [20]. The outer spikes have not been observed for pristine Bi_2Te_3. The scatterings *via* $\boldsymbol{q}_1$ (indicated in the CEC in Fig. 6d) along the $\bar{\Gamma}$-$\bar{K}$ direction are forbidden due to time-reversal symmetry. Therefore, our observed features along the $\bar{\Gamma}$-$\bar{K}$ direction in Figs. 5d-h require new scattering channels that will be discussed below based on DFT calculations. As the voltage increases, our QPI mapping at 200-300 mV shows interference patterns only along the $\bar{\Gamma}$-$\bar{M}$ direction (referred to as *open* hexagonal patterns in order to differentiate from the features at lower voltages) without apparent secondary outer spikes.

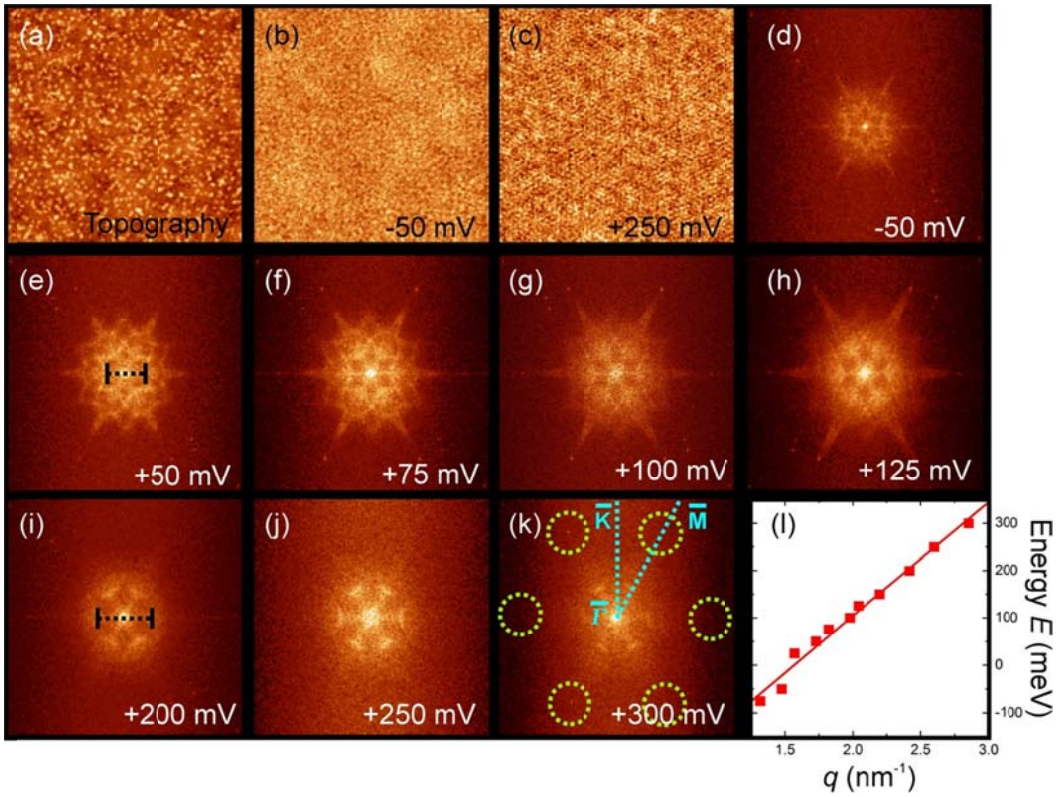

Figure 5: QPI mapping. (a) 60 x 60 nm^2 STM topography of a Bi bilayer covered Bi_2Te_3 region (with about 300 defects per 1000 nm^2) at +50 mV. (b)-(c) Corresponding LDOS maps and (d)-(k) corresponding FT-QPI maps acquired at the indicated voltages. In (k) the distance between two opposing green dotted circles is 5.4 nm^{-1}, and the two blue dotted lines indicate the $\bar{\Gamma}$-$\bar{K}$ and $\bar{\Gamma}$-$\bar{M}$ directions. (l) Energy dispersion of the surface state determined from the FT-QPI images, together with a linear fitting result. T_{sample} = 4.5 K.

We now estimate the energy dispersion of the TSS electrons from the measured FT-QPI patterns. The prominent scatterings along the $\bar{\Gamma}$-$\bar{M}$ direction shown in Figs. 5d-k and in Refs. [12,13,20,27] are attributed to $\boldsymbol{q}_2$ in the CEC of Fig. 6d. The involved $\boldsymbol{k}_i$ and $\boldsymbol{k}_f$ are wave vectors that point along the $\bar{\Gamma}$-$\bar{K}$ direction because a higher density of surface states is found along this direction (Fig. 6d). Considering the scattering geometry in the CEC, $\boldsymbol{q}_2$ and $\boldsymbol{k}$ are related by $q = |\boldsymbol{q}_2| = \sqrt{3}\,k$. Green dotted circles in Fig. 5k highlight the six maxima obtained from the atomic structure of the Bi_2Te_3(111) surface. From the maxima we identified the $\bar{\Gamma}$-$\bar{K}$ and $\bar{\Gamma}$-$\bar{M}$ directions. The center of the FT-QPI map corresponds to the

center of the reciprocal lattice of the hexagonal lattice. The length of the 2D reciprocal lattice vectors is inferred as $\pi \cdot 5.4\ \mathrm{nm}^{-1}$. Based on the FT-QPI images in Figs. 5d-k and SM-7, we determined the energy dispersion of the surface states. Values of the wave vector are determined as half of the length of the bars along the $\bar{\Gamma}$-$\bar{M}$ direction, as indicated in Figs. 5e and 5i. Since STM measurements map the square of the electron (standing) wave function,[28] the value obtained from the FT-QPI images is in fact twice the quasiparticle wave vector $\boldsymbol{q}$. Note that we treated our FT-QPI images with a minor smoothing filter only, without symmetrizing operations.[29] The results are presented in Fig. 5l. The electronic features in the FT-QPI images clearly exhibit a linear dependence on the tunneling voltage. Its slope can be obtained by fitting the data points to a linear energy dispersion $E(k) = E_D + \hbar v_F k$.[12,30] We find the Dirac point energy E_D = -380 ± 20 meV and the Fermi velocity $v_F = (6.3 \pm 0.3) \times 10^5$ m/s. Note that the energy dispersion shows only minor dependence on the density of atomic defects (Fig. SM-9), similar to the above discussed vacuum level related resonance (Fig. SM-8).

To further investigate whether our experimental QPI features are compatible with a Bi bilayer covered Bi_2Te_3 system, we performed DFT-based calculations of the QPI patterns. Also, we identified the scattering channels giving rise to the aforementioned unique interference patterns at low voltages, when compared to the FT of QPI patterns for pristine Bi_2Te_3. The band structure of pristine Bi_2Te_3 and the Bi bilayer covered Bi_2Te_3 system is presented in Fig. 6a and Fig. 6b, respectively. The cone corresponding to the TSS state near the top of the valence band is indicated in red for Bi_2Te_3 and in blue for the Bi bilayer covered Bi_2Te_3 system. The Fermi level is chosen as the zero of energy in each case. One can clearly see that the Bi bilayer has resulted in a downward band bending, which is responsible for the shift in vacuum energy discussed above. This band bending shifts the TSS to higher binding energies, but a new ("second") cone-like band structure at the $\bar{\Gamma}$ point close to the top of valence band can be observed. This new Dirac cone was also mentioned in Refs. [31-33]. We identify that the new Dirac cone originates from the lowest conduction band state of the pristine system. We refer to Fig. SM-10

for details of the characteristics of the bands. This mechanism is similar to what was found for a Bi bilayer on top of Bi_2Se_3 studied in Ref. [8]. Our QPI calculations based on this cone-like band structure (indicated in blue in Fig. 6b) do show closed hexagonal QPI patterns starting from energy E = 120 meV, as shown in Fig. 6c. Furthermore, the length of the $\boldsymbol{q}_2$ vector in the corresponding CEC (Fig. 6d) is about 1.5 nm^{-1}, in agreement with the experimental QPI at -50 mV. The scattering processes responsible for the QPI feature along the $\bar{\Gamma}$-$\bar{K}$ direction occur *via* $\boldsymbol{q}_3$ in Fig. 6d. These processes are more pronounced in the Bi bilayer covered Bi_2Te_3 than in the pristine Bi_2Te_3, when we consider the peculiar curvature of the CEC, such as stronger hexagonal warping (sharply peaked in the $\bar{\Gamma}$-$\bar{M}$ direction) and smoothly curved in the $\bar{\Gamma}$-$\bar{K}$ direction, in combination with the fact that the spin is still approximately tangential to this CEC (see discussion of Fig. 6i below).

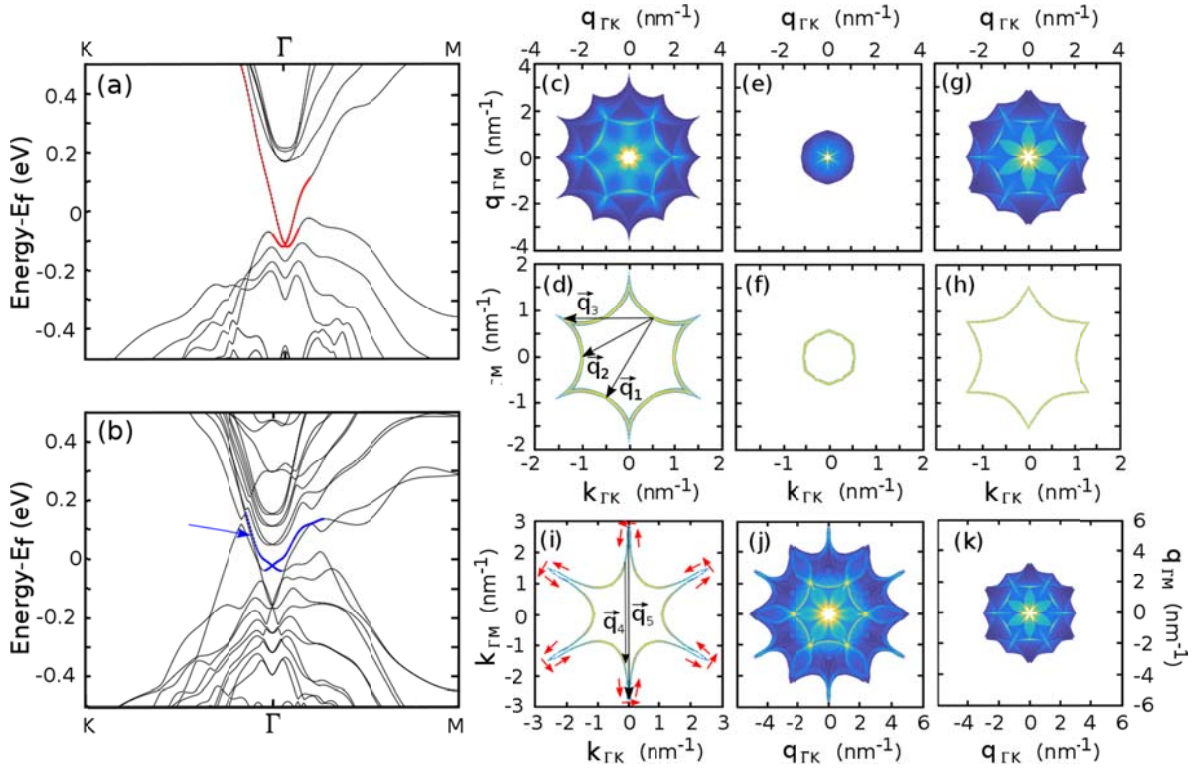

Figure 6: Theoretical study of the Bi bilayer on Bi_2Te_3 system *versus* pristine Bi_2Te_3. (a) DFT-calculated band structure of the QL-terminated Bi_2Te_3, where the TSSs are indicated in red. (b) DFT-calculated band structure of the Bi-bilayer adsorbed on Bi_2Te_3, where the new cone-like

band structure is marked in blue. (c) and (d) represent the CEC and the QPI pattern of the Bi bilayer covered Bi_2Te_3 surface, respectively, obtained at 120 meV above the Fermi level (*i.e.*, 135 meV above the blue Dirac point in (b)). (e) and (f) represent the CEC and the QPI pattern of the bare Bi_2Te_3 surface, respectively, obtained at 20 meV above the Fermi level (*i.e.*, 135 meV above the red Dirac point in (a)). (g) and (h) represent the CEC and the QPI pattern of the bare Bi_2Te_3 surface, respectively, obtained at 155 meV above the Fermi level (*i.e.*, 270 meV above the red Dirac cone in (a)). (i) and (j) CEC and QPI pattern of the Bi bilayer covered Bi_2Te_3 surface, obtained at 150 meV above the Fermi level. The red arrows indicate the schematic spin structure. (k) QPI pattern of the bare Bi_2Te_3 surface, obtained at 185 meV above the Fermi level.

As noted earlier, the fitted energy dispersion in Fig. 5l is based on the length of vector $\boldsymbol{q}_2 = \boldsymbol{k}_f - \boldsymbol{k}_i$ that is oriented along the $\bar{\Gamma}$-$\bar{M}$ direction (Figs. 5i and 6d), while the constituting $\boldsymbol{k}_i$ and $\boldsymbol{k}_f$ are oriented along the $\bar{\Gamma}$-$\bar{K}$ direction. Therefore, the energy dispersion in Fig. 5l should correspond to the energy branch in the $\bar{\Gamma}$-$\bar{K}$ direction of the Bi bilayer covered Bi_2Te_3 system, indicated by the arrow in the band structure of Fig. 6b. The calculated slope of the band at E = 120 meV leads to a Fermi velocity of about 4.3 10^5 m/s. Note that this velocity is similar to the calculated Fermi velocity of the red Dirac cone of pure Bi_2Te_3. Extrapolating this (blue) band further down, it crosses the $\bar{\Gamma}$ point around E_e = -150 meV. Thus, the energy of 120 meV at which the QPI and CEC were calculated (Figs. 6c-d) corresponds to an energy of 270 meV above E_e. The energy at which the experimental QPI was obtained, -50 meV, is equivalent to 330 meV ± 20 meV above the fitted Dirac point E_D, which is in reasonable agreement with the calculated result.

Interestingly, this closed hexagonal shape of the calculated QPI already appears only 135 meV above the Dirac point of the blue cone, E_b = -15 meV. It is now instructive to see how the QPI and CEC would look for pure Bi_2Te_3 at 135 meV above the red Dirac point, E_r = -115 meV. The QPI pattern and corresponding CEC are shown in Figs. 6e-f, respectively. It is clear that the QPI and CEC for the TSS

of the pristine Bi_2Te_3 evolve much more slowly with increasing energy than for the "second" cone of the Bi bilayer covered Bi_2Te_3 system. Finally, we show the QPI pattern and CEC for pure Bi_2Te_3 at 270 meV above the E_r value in Fig. 6g and in Fig. 6h, respectively. This corresponds to E = 155 meV from the Fermi level. Some features along the $\bar{\Gamma}$-$\bar{K}$ direction are found, but less pronounced. Furthermore, a truly closed hexagonal shape is never found for the pure Bi_2Te_3 system, while it clearly exists for the Bi bilayer covered Bi_2Te_3 system. As an example, Fig. 6j and Fig. 6k present the QPIs for the Bi bilayer covered Bi_2Te_3 system and Bi_2Te_3, respectively, at an extra 30 meV above the ones shown in Fig. 6c and Fig. 6g: for E = 120 meV + 30 meV = 150 meV for the Bi bilayer covered Bi_2Te_3 system, and for E = 155 meV + 30 meV = 185 meV for Bi_2Te_3. For the Bi bilayer covered Bi_2Te_3 system, the closed hexagonal structure is very pronounced, even a second outer shape can be identified, as in the experimental QPI patterns (Fig. 5e). This second outer shape is caused by scattering processes like $\boldsymbol{q}_4$, indicated in the CEC of the Bi bilayer covered Bi_2Te_3 at 150 meV in Fig. 6i . The red arrows indicate schematically the spin texture based on DFT calculations. The vector $\boldsymbol{q}_4$ is slightly off from the tips of the contour. Due to the extremely sharp contour shape, the tangential spin texture shows that scattering by the $\boldsymbol{q}_4$ vector is enhanced, while scattering by the $\boldsymbol{q}_5$ vector (from one tip to the opposite tip) is forbidden by time-reversal symmetry. It could be tempting to identify the calculated QPI for pure Bi_2Te_3 in Fig. 6j with the QPI measured at a tunneling voltage of +250 mV. However, the Fermi level of this calculated QPI at E = 185 meV is only 300 meV above the E_r value, while the measured one is estimated to be 380 + 250 meV = 630 meV above the E_D value. Furthermore, at a voltage of +250 mV, the length of the $\boldsymbol{q}_2$ vector is measured to be aroud 2.6 nm^{-1} (Fig. 5l), while in the calculated QPI it is still below 2.0 nm^{-1} (Fig. 6k).

Based on the DFT calculations of the QPI patterns, we conclude that the experimental QPI patterns are consistent with a system in which a Bi bilayer is located on top of Bi_2Te_3 and that there is a better match between the calculations and the experiment for the Bi bilayer covered Bi_2Te_3 system than for a

pure Bi_2Te_3 system. All the observations based on the DFT calculations discussed above are a consequence of the different shape of the CEC and corresponding spin texture for Bi bilayer covered Bi_2Te_3 and pure Bi_2Te_3: The CEC of Bi bilayer covered Bi_2Te_3 is smoother along the $\bar{\Gamma}$-$\bar{K}$ direction and at the same time stronger hexagonal warping exists along the $\bar{\Gamma}$-$\bar{M}$ direction. We could not retrieve the QPI patterns observed in the experiments at 200-300 mV (Figs. 5g-i) because at such high energies it becomes very difficult to select the states from the band structure calculation that are probed in the STM measurement.

Conclusions

Relying on STM and AES experiments and on DFT-based calculations we demonstrated that the surface electronic band structure of Bi_2Te_3 crystals can be modified by an effective annealing procedure under UHV conditions. The annealing gives rise to restructuring of the Bi_2Te_3 surface, yielding a Bi(111) bilayer at the otherwise atomically flat terraces. The adlayer results in *n*-type doping and the atomic defects act as scattering centers of the TSS electrons, allowing to probe the modified TSS dispersion *via* QPI mapping. Our experimental FT-QPI patterns reveal considerably more features than FT-QPI patterns reported for pristine Bi_2Te_3: we observe *closed* hexagonal QPI patterns and secondary outer spikes. DFT calculations capture the experimental findings and can attribute the complex FT-QPI patterns to a modified constant-energy contour for the Bi bilayer covered surface. Due to charge transfer from the Bi bilayer towards the surface of Bi_2Te_3, a "second" cone was probed in the QPI mapping instead of the original TSS cone. The observed annealing-induced doping may be applicable to other topological materials and may offer a facile route for tuning of the topological properties.

Methods

Sample preparation. Crystals of Bi_2Te_3 were prepared by melting high-purity Bi and Te powders (5N, all from Alfa Aesar) and annealing in sealed quartz ampoules, as described in Ref. [34]. The temperature was rapidly increased to 850°C, which was kept for two days, and the mixture was stirred continuously to avoid ingredients segregation. After that, the temperature was decreased to 500°C to allow the crystalline nucleation in 5 days. A 5 days annealing from 500°C to 420°C finalized the preparation before dropping down to room temperature. The temperature-dependent resistivity of the pristine Bi_2Te_3 sample that is discussed in the main text is presented in the Supplemental Material (SM) in Fig. SM-2 and reveals a metallic resistance *versus* temperature dependence, both prior to and after UHV annealing treatment. All measurements presented in the main text are obtained on the same sample. The SM also includes data obtained on two other samples (Figs. SM-3 and SM-4).

STM experiments. Annealing experiments were conducted in a UHV system (base pressure in the low 10^{-9} mbar range) that is connected to a low-temperature STM (Omicron Nanotechnology) operated at 4.5 K (base pressure in the 10^{-11} mbar range). (dI/dV)(V) spectra and dI/dV maps (referred to as LDOS maps) were acquired by lock-in detection with open and closed feedback loop, respectively (unless mentioned otherwise), at 800Hz (amplitude is typically about 20 mV). STM data in this work were obtained with mechanically cut PtIr (10% Ir) STM tips, and with polycrystalline W tips that were electrochemically etched and cleaned *in situ* by thermal treatment. All bias voltages mentioned are with respect to the sample, and the STM tip was virtually grounded. The STM images were analyzed using the Nanotec WSxM software.[35] The annealing experiments presented in Fig. SM-3 are obtained in another UHV STM (Unisoku – Nanoscore gmbh) that is operated at room temperature (base pressure in the 10^{-11} mbar range).

AES experiments. The AES equipment (Thermofisher, Alpha 110 Channeltron Assembly) was used with an electron voltage of 8 kV and a filament current of 2 A. The pressure in the chamber was 4×10^{-9} mbar. The step size for data collection was 1 eV and the spot size is estimated to be 1 mm^2. Avantage v5.951 (Thermo) software was applied to obtain a quantitative analysis of the composition of the surface as described in Ref. [36].

Calculations. DFT calculations on Bi_2Te_3 were carried out by using DFT code, VASP,[37,38] within the generalized gradient approximation (GGA)[39] for an exchange-correlation functional and with projector-augmented wave (PAW) pseudopotentials.[40] Spin-orbit coupling was considered self-consistently within the DFT calculations. For the QL-terminated Bi_2Te_3 slab, we considered 5 QLs, while for the adlayer covered Bi_2Te_3 slabs, we considered adlayers on 5 QLs. Regarding the DFT calculations to obtain the work functions and DOS, we used the experimental lattice constants.[15] For the sub-QL terminated slabs (5 QLs with adlayers), only the vertical distances near the interface are relaxed with an energy cutoff of 250 eV and k-mesh of 11x11x1 points. For the computation of the QPI patterns, we relaxed the whole structure including van der Waals interaction by applying the optB86b-vdW density functional.[41] In this case, we used an energy cutoff of 300 eV and a 16x16x1 k-mesh grid. For all the DFT calculations, a thick vacuum layer of 20-30 Å was included in the supercell. The QPI patterns were obtained based on the DFT band structure and joint DOS approximation,[42] as explained in Ref. [11]. The electron spin was approximated from the calculated expectation values projected onto individual atoms implemented in VASP.

ACKNOWLEDGMENTS

The research in Leuven and Antwerp has been supported by the Research Foundation - Flanders (FWO, Belgium). The research in Leuven received additional support from the Flemish Concerted Research

Action program (BOF KU Leuven, Project No. GOA/14/007) and the KU Leuven project GOA "Fundamental challenges in Semiconductor Research". Z.L. acknowledges the support from the China Scholarship Council (No. 2011624021) and from KU Leuven Internal Funds (PDM). K. Schouteden and J. Debehets acknowledge additional support from the FWO. T. Chen and F. Song acknowledge the financial support of the National Key Projects for Basic Research of China (Grant Nos:2013CB922103, 2011CB922103), the National Natural Science Foundation of China (Grant Nos: 91421109, 11134005, 11522432, and 11274003), the Natural Science Foundation of Jiangsu Province (Grant BK20130054), and the Fundamental Research Funds for the Central Universities. K. Park was supported by U.S. National Science Foundation DMR-1206354 and San Diego Supercomputer Center (SDSC) Comet and Gordon under DMR060009N.

SUPPORTING INFORMATION AVAILABLE

Additional STS d*I*/d*V* data near the Fermi level, temperature-dependent resistivity measurement, STM topographies of detailed annealing session, STM topography step height profiles, dependence of the vacuum level on the density of defects, dispersion for regions with different density of defects, and additional DFT calculations. This material is available free of charge *via* the Internet at http://pubs.acs.org.

AUTHOR INFORMATION

Corresponding Author

Email: koen.schouteden@fys.kuleuven.be;

Author contributions

STM experiments by K.S., Z.L., U.T., and A.N. Auger experiments by J.D. Sample production by T.C. Calculations by K.G., K.P., and B.P. Supervision by F.S., D.L., B.P., and C. Van H. All authors discussed the results and participated in writing the manuscript.

Notes

The authors declare no competing financial interest.

References

(1) Zhang, H.; Liu, C.-X.; Qi, X.-L.; Dai, X.; Fang, Z.; Zhang, S. C. Topological Insulators in Bi_2Se_3, Bi_2Te_3, and Sb_2Te_3 With a Single Dirac Cone on the Surface. *Nat. Phys.* **2009,** 5, 438-442.

(2) Teweldebrhan, D.; Goyal, V.; Rahman, M.; Balandina, A. A. Atomically-Thin Crystalline Films and Ribbons of Bismuth Telluride. *Appl. Phys. Lett.* **2010**, 96, 053107.

(3) Urazhdin, S.; Bilc, D.; Mahanti, S. D.; Tessmer, S. H.; Kyratsi, T.; Kanatzidis, M. G. Surface Effects in Layered Semiconductors Bi_2Se_3 and Bi_2Te_3. *Phys. Rev. B* **2004,** 69, 085313.

(4) Teweldebrhan, D.; Goyal, V.; Balandin, A. A. Exfoliation and Characterization of Bismuth Telluride Atomic Quintuples and Quasi-Two-Dimensional Crystals. *Nano Lett.* **2010,** 10, 1209-1218.

(5) Coelho, P. M.; Ribeiro, G. A. S.; Malachias, A.; Pimentel, V. L.; Silva, W. S.; Reis, D. D.; Mazzoni, M. S. C.; Magalhães-Paniago, R. Temperature-Induced Coexistence of a Conducting Bilayer and the Bulk-Terminated Surface of the Topological Insulator Bi_2Te_3. *Nano Lett.* **2013,** 13, 4517-4521.

(6) He, X.; Zhou, W.; Wang, Z. Y.; Zhang, Y. N.; Shi, J.; Wu, R. Q.; Yarmoff, J. A. Surface Termination of Cleaved Bi_2Se_3 Investigated by Low Energy Ion Scattering. *Phys. Rev. Lett.* **2013,** 110, 156101.

(7) Edmonds, M. T.; Hellerstedt, J. T.; Tadich, A.; Schenk, A.; O'Donnell, K. M.; Tosado, J.; Butch, N. P.; Syers, P.; Paglione, J.; Fuhrer, M. S. Stability and Surface Reconstruction of Topological Insulator Bi_2Se_3 on Exposure to Atmosphere. *J. Phys. Chem. C* **2014,** 118, 20413−20419.

(8) Govaerts, K.; Park, K.; De Beule, C.; Partoens, B.; Lamoen, D. The Effect of Bi Bilayers on the Topological States of Bi_2Se_3: a First-Principles Study. *Phys. Rev. B* **2014,** 90, 155124.

(9) Govaerts, K.; Sluiter, M. H. F.; Partoens, B.; Lamoen, D. Homologous Series of Layered Structures in Binary and Ternary Bi-Sb-Te-Se Systems: *Ab Initio* Study. *Phys. Rev. B* **2014,** 89, 054105.

(10) Hewitt, A. S.; Wang, J.; Boltersdorf, J.; Maggard, P. A.; Dougherty, D. B. Coexisting Bi and Se Surface Terminations of Cleaved Bi_2Se_3 Single Crystals. *J. Vac. Sci. Technol. B* **2014,** 32, 04E103.

(11) Eich, A.; Michiardi, M.; Bihlmayer, G.; Zhu, X.-G.; Mi, J.-L.; Iversen, B. Bo; Wiesendanger, R.; Hofmann, Ph.; Khajetoorians, A. A.; Wiebe, J. Intra- and Interband Electron Scattering in a Hybrid Topological Insulator: Bismuth Bilayer on Bi_2Se_3. *Phys. Rev. B* **2014,** 90, 155414.

(12) Zhang, T.; Cheng, P.; Chen, X.; Jia, J.-F.; Ma, X.; He, K.; Wang, L.; Zhang, H.; Dai, X.; Fang, Z.; Xie, X.; Xue, Q.-K. Experimental Demonstration of Topological Surface States Protected by Time-Reversal Symmetry. *Phys. Rev. Lett.* **2009,** 103, 266803.

(13) Beidenkopf, H.; Roushan, P.; Seo, J.; Gorman, L.; Drozdov, I.; Hor, Y. S.; Cava, R. J.; Yazdani, A. Spatial Fluctuations of Helical Dirac Fermions on the Surface of Topological Insulators. *Nat. Phys.* **2011, 7**, 939-943.

(14) Sessi, P.; Bathon, T.; Kokh, K. A.; Tereshchenko, O. E.; Bode, M. Probing the Electronic Properties of Individual MnPc Molecules Coupled to Topological States. *Nano Lett.* **2014,** 14, 5092−5096.

(15) Nakajima, S. The Crystal Structure of $Bi_2Te_{3-x}Se_x$. *J. Phys. Chem. Solids* **1963,** 24, 479-485.

(16) http://www.lesker.com/newweb/deposition_materials/materialdepositionchart.cfm?pgid=0. Date of access: May 2016.

(17) Powell, C. J.; Seah, M. P. Precision, Accuracy, and Uncertainty in Quantitative Surface Analyses by Auger-Electron Spectroscopy and X-Ray Photoelectron Spectroscopy. *J. Vac. Sci. Technol. A* **1990,** 2, 735-763.

(18) Haneman, M. Photoelectric Emission and Work Functions of InSb, GaAs, Bi_2Te_3 and Germanium. *J. Phys. Chem. Solids* **1959,** 11, 205-214.

(19) Binnig, G.; Frank, K. H.; Fuchs, H.; Garcia, N.; Reihl, B.; Rohrer, H.; Salvan, F.; Williams, A. R. Tunneling Spectroscopy and Inverse Photoemission: Image and Field States. *Phys. Rev. Lett.* **1985,** 55, 991-994.

(20) Sessi, P.; Otrokov, M. M.; Bathon, T.; Vergniory, M. G.; Tsirkin, S. S.; Kokh, K. A.; Tereshchenko, O. E.; Chulkov, E. V.; Bode, M. Visualizing Spin-Dependent Bulk Scattering and Breakdown of the Linear Dispersion Relation in Bi_2Te_3. *Phys. Rev. B* **2013,** 88, 161407(R).

(21) Park, K.; De Beule, C.; Partoens, B. The Ageing Effect in Topological Insulators: Evolution of the Surface Electronic Structure of Bi_2Se_3 Upon K Adsorption. *New J. Phys*. **2013,** 15, 113031.

(22) Yeom, H. W.; Kim, S. H.; Shin, W. J.; Jin, K.-H.; Park, J.; Kim, T.-H.; Kim, J. S.; Ishikawa, H.; Sakamoto, K.; Jhi, S.-H. Transforming a Surface State of a Topological Insulator by a Bi Capping Layer. *Phys. Rev. B* **2014,** 90, 235401.

(23) Jin, K.-H.; Yeom, H. W.; Jhi, S.-H. Band Structure Engineering of Topological Insulator Heterojunctions. *Phys. Rev. B* **2016,** 93, 075308.

(24) Chen, M.; Peng, J.-P.; Zhang, H.-M.; Wang, L.-L.; He, K.; Ma, X.-C.; Xue, Q.-K. Molecular Beam Epitaxy of Bilayer Bi(111) Films on Topological Insulator Bi_2Te_3: A Scanning Tunneling Microscopy Study. *Appl. Phys. Lett.* **2012,** 101, 081603.

(25) Niesner, D.; Otto, S.; Fauster, Th.; Chulkov, E. V.; Eremeev, S. V.; Tereshchenko, O. E.; Kokh, K. A. Electron Dynamics of Unoccupied States in Topological Insulators. *J. Electron Spectrosc. Relat. Phenom.* **2014, 195**, 258-262.

(26) Alpichshev, Z.; Analytis, J. G.; Chu, J.-H.; Fisher, I. R.; Chen, Y. L.; Shen, Z. X.; Fang, A.; Kapitulnik, A. STM Imaging of Electronic Waves on the Surface of Bi_2Te_3: Topologically Protected Surface States and Hexagonal Warping Effects. *Phys. Rev. Lett.* **2010,** 104, 016401.

(27) Zhou, W. *STM Probe on the Surface Electronic States of Spin-Orbit Coupled Materials*. PhD Thesis, Boston College University Libraries **2014**. Available at http://hdl.handle.net/2345/bc-ir:103564

(28) Petersen, L.; Sprunger, P. T.; Hofmann, Ph.; Lægsgaard, E.; Briner, B. G.; Doering, M.; Rust, H.-P.; Bradshaw, A. M.; Besenbacher, F.; Plummer, E. W. Direct Imaging of the Two-Dimensional Fermi Contour: Fourier-Transform STM. *Phys. Rev. B* **1998,** 57, R6858.

(29) Mann, C. Commentary on the Interpretation of Fourier-Transform Scanning Tunneling Microscopy Data. *arXiv.org, e-Print Arch., Condens. Matter* arXiv:1509.07807 [cond-mat.mtrl-sci], **2015**.

(30) Hsieh, D.; Qian, D.; Wray, L.; Xia, Y.; Hor, Y. S.; Cava, R. J.; Hasan, M. Z. A Topological Dirac Insulator in a Quantum Spin Hall Phase. *Nature* **2008,** 452, 970-975.

(31) Hirahara, T.; Bihlmayer, G.; Sakamoto, Y.; Yamada, M.; Miyazaki, H.; Kimura, S.; Blügel, S.; Hasegawa, S. Interfacing 2D and 3D Topological Insulators: Bi(111) Bilayer on Bi_2Te_3. *Phys. Rev. Lett.* **2011,** 107, 166801.

(32) Miao, L.; Yao, M.-Y.; Ming, W.; Zhu, F.; Han, C. Q.; Wang, Z. F.; Guan, D. D.; Gao, C. L.; Liu, C.; Liu, F.; Qian, D.; Jia, J.-F. Evolution of the Electronic Structure in Ultrathin Bi(111) Films. *Phys. Rev. B* **2015,** 91, 205414.

(33) Yang, F.; Miao, L.; Wang, Z. F.; Yao, M.-Y.; Zhu, F.; Song, Y. R.; Wang, M.-X.; Xu, J.-P.; Fedorov, A. V.; Sun, Z.; Zhang, G. B.; Liu, C.; Liu, F.; Qian, D.; Gao, C. L.; Jia, J.-F. Spatial and Energy Distribution of Topological Edge States in Single Bi(111) Bilayer. *Phys. Rev. Lett.* **2012,** 109, 016801.

(34) Chen, T.; Chen, Q.; Schouteden, K.; Huang, W.; Wang, X.; Li, Z.; Miao, F.; Wang, X.; Li, Z.; Zhao, B.; Li, S.; Song, F.; Wang, J.; Wang, B.; Van Haesendonck, C.; Wang, G. Topological Transport and Atomic Tunneling-Clustering Dynamics for Aged Cu-Doped Bi_2Te_3 Crystals. *Nat. Commun.* **2014,** 5, 5022.

(35) Horcas, I.; Fernández, R.; Gómez-Rodríguez, J. M.; Colchero, J.; Gómez-Herrero, J.; Baro, A. M. WSxM: A Software for Scanning Probe Microscopy and a Tool for Nanotechnology. *Rev. Sci. Instrum.* **2007,** 78, 013705.

(36) Debehets, J.; Miranda, S. M. C.; Homm, P.; Houssa, M.; Seefeldt, M.; Locquet, J. P.; Seo, M. Auger Electron Spectroscopy Study of Semiconductor Surfaces: Effect of Cleaning in Inert Atmosphere. *J. Vac. Sci. Technol. B* **2016,** 34, 041227.

(37) Kresse, G.; Furthmüller, J. Efficient Iterative Schemes for *Ab Initio* Total-Energy Calculations Using a Plane-Wave Basis Set. *Phys. Rev. B* **1996,** 54, 11169-11186.

(38) Kresse, G.; Furthmüller, J. Efficiency of Ab-Initio Total Energy Calculations for Metals and Semiconductors Using a Plane-Wave Basis Set. *Comp. Mater. Sci.* **1996,** 6, 15-50.

(39) Perdew, J. P.; Burke, K.; Ernzerhof, M. Generalized Gradient Approximation Made Simple. *Phys. Rev. Lett*. **1996, 77**, 3865.

(40) Blöchl, P. E. Projector Augmented-Wave Method. *Phys. Rev. B* **1994,** 50, 17953-17979.

(41) Klimes, K.; Bowler, D. R.; Michaelides, A. Van der Waals Density Functional Applied to Solids. *Phys. Rev. B* **2011,** 83, 195131.

(42) Simon, L.; Bena, C.; Vonau, F.; Cranney, M.; Aubel, D. Fourier-Transform Scanning Tunneling Spectroscopy: The Possibility to Obtain Constant-Energy Maps and Band Dispersion Using a Local Measurement. *J. Phys. D: Appl. Phys.* **2011,** 44, 464010.

(43) Childs, K. D.; Carlson, B. A.; LaVanier, L. A.; Moulder, J. F.; Paul, D. F.; Stickle, W. F.; Watson. D. G. Handbook of Auger electron spectroscopy. Physical Electronics, Eden Prairie (1995).

Graphical Table of Contents entry:

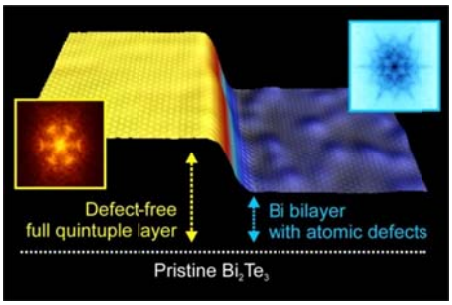

Description: Atomically resolved topography after annealing of Bi_2Te_3 under ultra-high-vacuum conditions. The annealing leads to the formation of a Bi bilayer atop the pristine Bi_2Te_3 surface. In the image a quintuple layer step separates a pristine region from a Bi bilayer-covered region. The obtained surfaces are investigated *via* quasi-particle interference mapping (insets), revealing complex star-shaped features for the bilayer region. Image size is 25 x 10 nm^2. The image contrast was optimized using Fourier filtering techniques.

Supplemental Material for Article "Annealing-Induced Bi Bilayer on Bi_2Te_3 Investigated *Via* Quasi-Particle-Interference Mapping"

Koen Schouteden[a]*, Kirsten Govaerts[b], Jolien Debehets[c], Umamahesh Thupakula[a], Taishi Chen[d], Zhe Li[a], Asteriona Netsou[a], Fengqi Song[e], Dirk Lamoen[b], Chris Van Haesendonck[a], Bart Partoens[b], and Kyungwha Park[f]

a) Solid-State Physics and Magnetism Section, KU Leuven, BE-3001 Leuven, Belgium

b) EMAT and CMT group, Department of Physics, Universiteit Antwerpen, B-2020 Antwerpen, Belgium

c) Department of Materials Engineering, KU Leuven, BE-3001 Leuven, Belgium

d) Max Planck Institute for Chemical Physics of Solids, Dresden, Germany

e) National Laboratory of Solid State Microstructures, Collaborative Innovation Center of Advanced Microstructures, and Department of Physics, Nanjing University, Nanjing 210093, China

f) Department of Physics, Virginia Tech, Blacksburg, Virginia 24061, USA

* koen.schouteden@fys.kuleuven.be

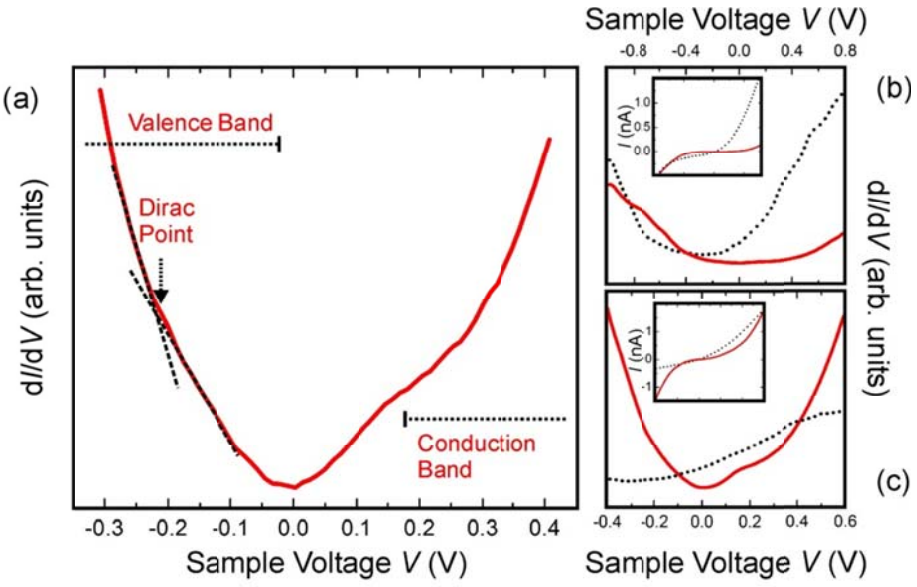

Figure SM-1: Spectroscopy near the Fermi level. (a) Area-averaged d*I*/d*V* spectrum (including about 100 single spectra) of the pristine Bi_2Te_3 surface shown in Fig. 2a. The spectrum is consistent with previously reported spectra in Refs. [1-3]. Assignment of the valence band maximum, conduction band minimum and Dirac point is done following Ref. [1], *i.e.*, by the minimum in the d*I*/d*V* curve, the shoulder at 180 meV, and the (small) change of the slope in the d*I*/d*V* curve below the Fermi level, respectively. In Ref. [1], the authors attribute the small shift in the d*I*/d*V* curve with respect to the curve reported in Ref. [3] to different sample doping. Setpoint values used are V = -1.0 V and I = 0.2 nA. Lock-in modulation amplitude is 20 mV. (b) Red spectrum is the same spectrum as in (a), yet taken in a larger voltage range. Black dotted spectrum is taken on the neighboring Bi bilayer covered Bi_2Te_3 region shown in Fig. 2a and reveals a broad minimum in the -0.2 to -0.4 V range. (c) d*I*/d*V* spectra of the same regions at different setpoint values: V = +0.6 V and I = 0.6 nA. Insets in (b) and (c) show the corresponding $I(V)$ spectra. The $I(V)$ spectra show clear non-linear behavior, implying that for comparison of the two regions normalized $(dI/dV)*(I/V)^{-1}$ spectra are preferred (see Fig. 2c). Lock-in modulation amplitude is 30 mV. T_{sample} = 4.5 K.

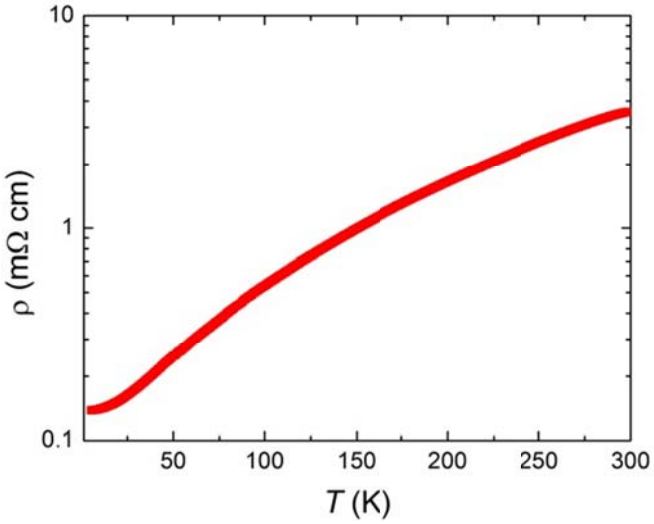

Figure SM-2: Temperature-dependent resistivity. Temperature-dependent resistivity of the Bi_2Te_3 sample that is discussed in the main text. This measurement allows to check the bulk conductivity and reveals a metallic resistance *versus* temperature dependence, both prior to (shown in figure) and after the annealing sessions (data not shown) that are discussed in the manuscript. The crystalline order of the Bi_2Te_3 crystal was verified by X-ray powder diffraction and transmission electron microscopy and has been previously reported in Ref. [4].

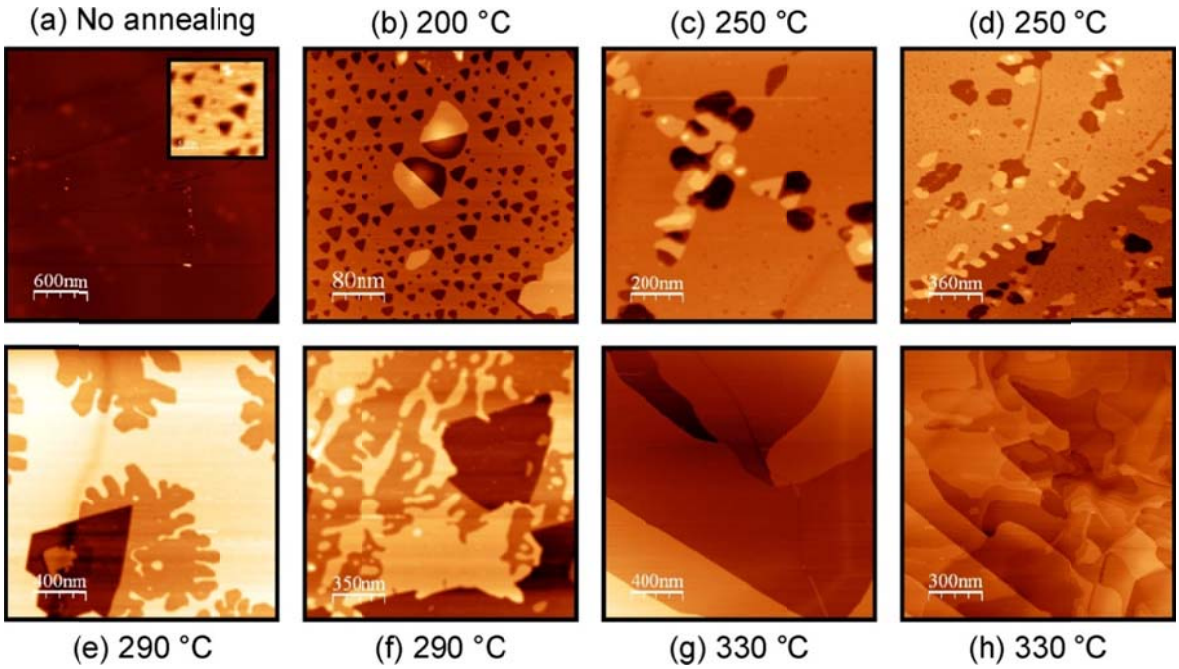

Figure SM-3: Detailed annealing session. Series of STM topographies of another Bi_2Te_3 surface (different from the one discussed in the main text) after annealing in UHV to the indicated temperatures. The surface topography changes gradually with increasing annealing temperature: Small defects/protrusions/depressions aggregate [(b)-(d)] and the QL steps reorganize [(e)-(f)]. At higher temperatures atomic defects appear and step heights are typically below that of a QL. These changes are attributed to surface restructuring and desorption of Te from the top QL. The annealing effects can be expected to take place first at regions of the sample that have a high density of (sub-QL) steps, which may explain the local variations of the sample topography observed after annealing as illustrated in (g) and (h). Step edges typically are subject the most to structural changes during annealing or manipulation experiments.[5] In general, the annealing behavior is similar for all investigated samples (6 in total). Differences between different samples are attributed to the different initial quality of the sample surface prior to annealing, which is determined by the mechanical exfoliation and adsorption of contamination during the brief exposure to air. T_{sample} = 300 K.

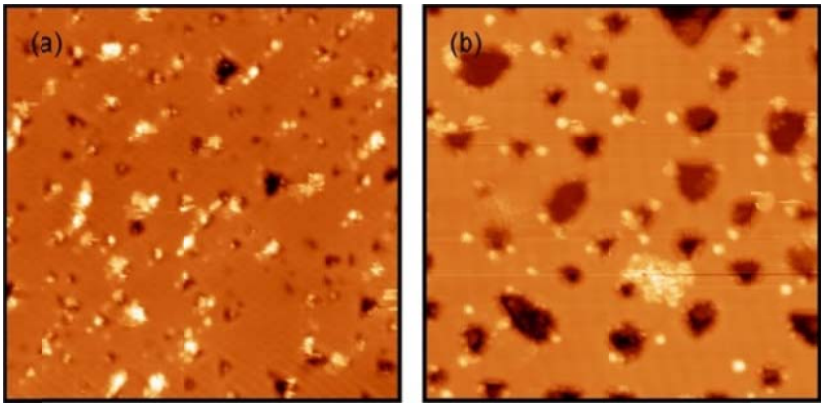

Figure SM-4: Annealing of another sample. 50 x 50 nm^2 STM topographies of the surface of another Bi_2Te_3 sample. The topographies of this sample (a) prior to and (b) after annealing to about 230°C are similar to that of the sample that is discussed in the main manuscript (see Figs. 1c and 1d). Surface cleanliness has improved considerably by annealing. Typical depth of the vacancy islands in (b) is 0.2-0.3 nm. The increased lateral size of the vacancy islands is attributed to surface restructuring and desorption of Te from the top QL. Setpoint values used are (a) V = +0.9 V and I = 0.3 nA and (b) (a) V = +1.0 V and I = 0.2 nA. T_{sample} = 4.5 K.

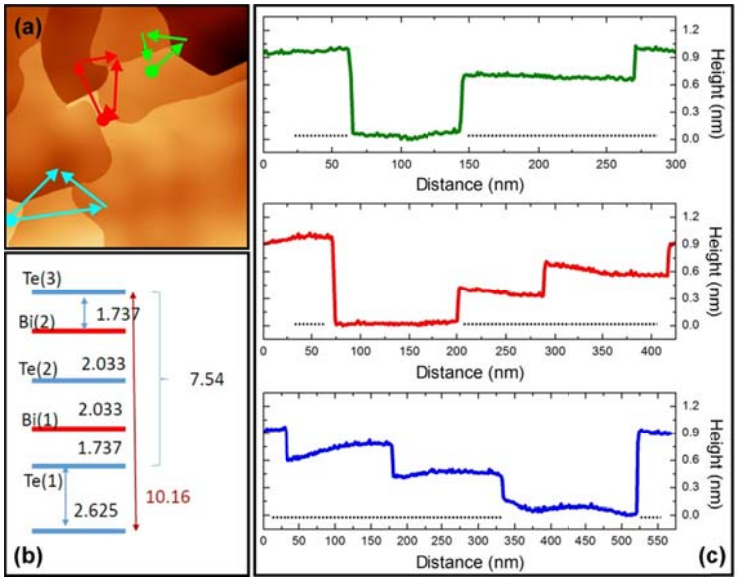

Figure SM-5: Step height profiles. (a) STM topography of a fully Bi bilayer covered region of the Bi_2Te_3 surface (sample that is discussed in the main text) with a high density of sub-QL steps after annealing to 433°C. Atomic defects are present everywhere in (a), from which we conclude that the entire surface in (a) is covered by a Bi bilayer. Image size is 600 x 600 nm^2. Setpoint values are V = +1.0 V and I = 0.05 nA. *Regions of the sample that have a high-density of sub-QL steps such as that in (a) typically do not show defect-free terraces (i.e., pristine Bi_2Te_3 terraces that have a vacuum level of 5.3 eV, see Fig. 2) and hence they have no well-defined reference surface. In the main text, we focus on regions that have a neighboring pristine Bi_2Te_3 terrace that allows us to identify the defect regions as Bi bilayer on top of a complete Bi_2Te_3 QL, similar to the region discussed in Fig. 2.* (b) Calculated heights of the Bi and Te intralayers within a QL. Superscripts (1) and (3) on one hand, and superscript (2) on the other hand, denote two different chemical states for the anions:[6] The outmost atoms Te(1) [Te(3)] are strongly bound (covalently or partially ionic) to three planar Te(1) [Te(3)] and three Bi metal atoms of the same quintuple layers, while they are weakly bound (mainly van der Waals) to three Te(3) [Te(1)] atoms of the next QL below (above). The van der Waals gap between the QLs yields a preferential cleavage between the adjacent Te(1)-Te(3) layers. (c) Three height profiles taken along the paths at the locations indicated in (a). As indicated above, for regions that do not have a neighboring pristine

surface, such as that in (a), these step height values in (c) cannot be unambiguously linked to a specific adlayer thickness or surface termination. For example, based on the values in (b), a step height of around 0.37 nm may be assigned to the height of a Te(3)-Bi(2) layer on Te(2), or to the height of a Te(2)-Bi(1) layer on Te(1). Note that the occurrence of intralayer QL terminations may have increased upon Te desorption as recently shown for Bi_2Te_3 films that were grown with varying Te concentration.[7] In addition, the high density of sub-QL steps may point to the existence of multiple Bi bilayers, which are known to have a height of about 0.39 nm.[8]

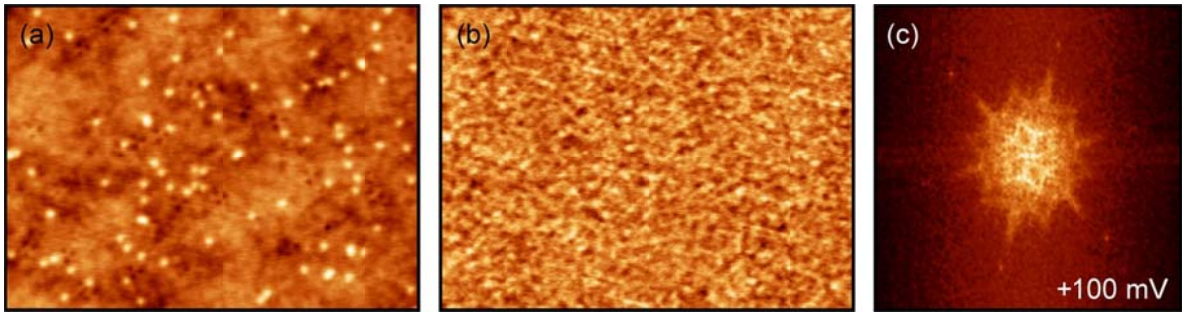

Figure SM-6: QPI mapping and Fourier transform. (a) 40 x 30 nm^2 STM topography of a Bi bilayer covered Bi_2Te_3 region (with about 100 defects per 1000 nm^2) recorded at +100 mV and (b) the corresponding QPI map. (c) Fourier-transform image of (b).

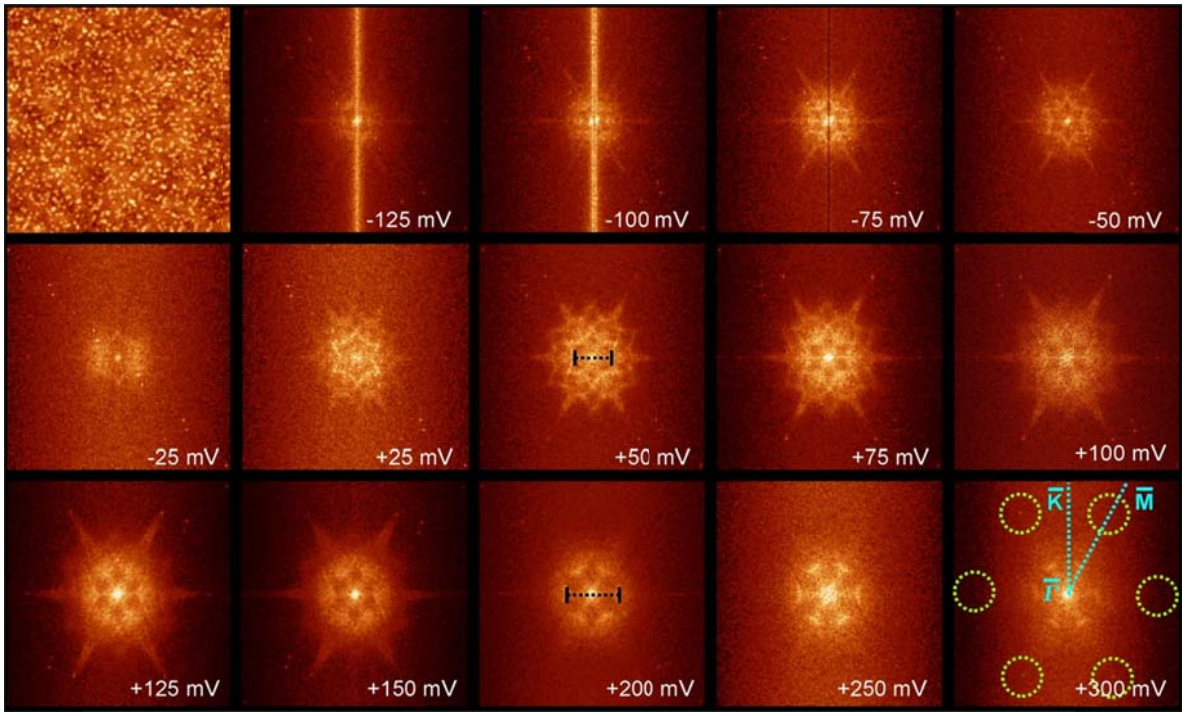

Figure SM-7: Series of FT-QPI maps. 60 x 60 nm^2 STM topography of the Bi bilayer covered Bi_2Te_3 region shown in Fig. 5a (with about 300 defects per 1000 nm^2) recorded at +50 mV, and corresponding series of Fourier-transform images of QPI maps acquired at the indicated voltages. The distance between two sets of maxima indicated by the green dotted circle in the +300 mV image is 5.4 nm^{-1}.

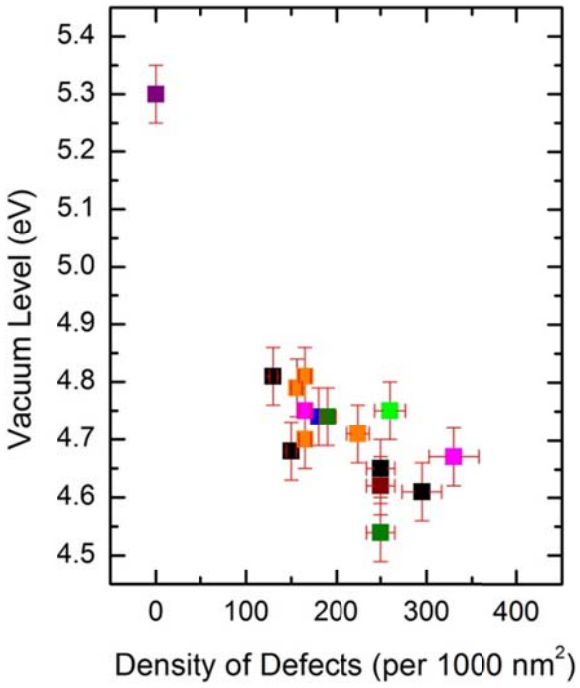

Figure SM-8: Dependence of the vacuum level on the density of defects. Vacuum level values obtained from STS spectra taken at different regions of the same Bi bilayer covered Bi_2Te_3 sample with a different density of defects. Setpoint values used are V = +0.2 V and I = 0.5 nA (T_{sample} = 4.5 K.). The (lock-in) modulation amplitude was 20 mV. Densities ranging from 10 to 400 defects per 1000 nm^2 are retrieved. The density does not vary significantly within one terrace, and mainly shows variation from terrace to terrace. Data can be interpreted as a downward shift that is mainly caused by the presence of the Bi bilayer, as discussed in the main text. In addition, there exists a small yet significant correlation between the observed vacuum level and the density of defects: the vacuum level shifts further to lower energies with increasing density of defects.

Figure SM-8 mainly includes data obtained on regions that have a high density of sub-QL steps and that exhibit defects everywhere. *As indicated in the caption of Fig. SM-5, regions of the sample that have a high-density of sub-QL steps such as that in (a) typically do not show defect-free terraces (i.e. pristine Bi_2Te_3 terraces that have a vacuum level of 5.3 eV, see Fig. 2) and hence they have no well-*

defined reference surface, which may at least partially explain the scattered data in Fig. SM-8. In the main text, we focus on regions that have a neighboring pristine Bi_2Te_3 terrace that allows us to identify the defect regions as Bi bilayer on top of a complete Bi_2Te_3 QL, similar to the region discussed in Fig. 2. The density of defects is always determined from an area of 40 x 40 nm^2. The experimental *x*-error value is taken as "$density^2$ * 0.0025" to reflect the increasing uncertainty of the density determination with increasing density of defects. At high densities, defects that are in very close proximity cannot be discerned and are counted as one defect in our analysis using the WSxM software.[9] The (systematic) experimental *y*-error value reflects the observed variation of the vacuum level when determined from different STS spectra taken within the same region. Each color in Fig. SM-8 represents a different "data set". Each data set (when consisting of two or more data points) reveals a lowering of the vacuum level with increasing density of defects. Each data set is obtained with the same STM tip, *i.e.*, no so-called tip change occurred in between measurements of one data set. A change of the tip apex leads to a different electric field between tip and sample (even when using the same setpoint values), which may additionally explain the scatter between the different data sets. The data point at zero density of defects (the pristine surface) is verified in three independent experiments.

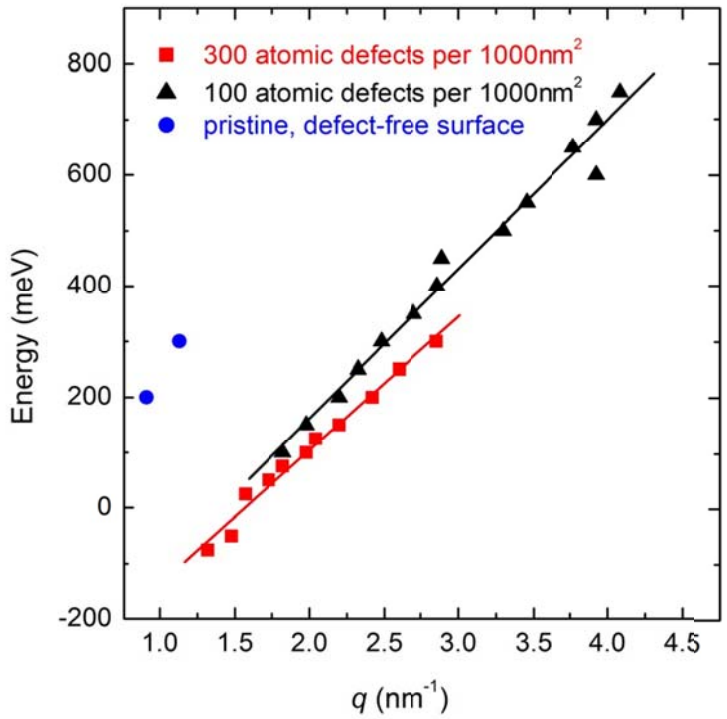

Figure SM-9: Dispersion for regions with different defect densities. Energy dispersion of the surface state of Bi_2Te_3 determined from Fourier-transform images of a region with 100 defects per 1000 nm^2 (topo shown in Fig. SM-6) and a region with 300 defects per 1000 nm^2 (see Fig. SM-7), together with a linear fitting result. Two data points of a pristine region were obtained at a QL step. T_{sample} = 4.5 K.

In the main text we showed that the vacuum level and other electronic features shift to lower energies due to the Bi bilayer. In Fig. SM-8, we showed that there exists also a small dependence on the density of defects in the Bi bilayer. In that view, one can expect that there exist differences in the surface state dispersion of regions with a different density of defects. We determined the energy-dispersion behavior of the QPI patterns in the Fourier-transform images for a region with 100 defects per 1000 nm^2 (one Fourier-transform image is presented in Fig. SM-6) and a region with 300 defects per 1000 nm^2 (Fourier-transform images are shown in Fig. SM-7). The Bi bilayer in Fig. SM-6 and in Fig. SM-7 both have a thickness around 0.4 nm, similar to the case of Fig. 2a. Values of the quasiparticle wave vector

$\boldsymbol{q}$ are determined as indicated in Fig. SM-7 (see the maps at +50 mV and + 200 mV) following the sixfold symmetric scattering vector in the $\bar{M}$ direction. The results are presented in Fig. SM-9. Two data points of a pristine region could be obtained at a QL step and are added as a reference. We find E_D = -380 ± 30 meV and v_F = 7.1 +/- 0.3 10^5 m/s for the 100 defects region, and E_D = -380 ± 20 meV and v_F = 6.3 ± 0.3 10^5 m/s for the 300 defects region. These Dirac point values are well below the Fermi level and are in line with the downward shifts of the electronic resonances. Fermi velocities are in reasonable agreement with previously reported values.[1,10] As mentioned above, a different value of the Dirac point is expected for regions with a different density of defects. From our STS results (see Fig. SM-8), these differences are expected to be rather small and are within the experimental error of our Dirac point determination relying on the linear dispersion relation. Nevertheless, it can be observed that the energy dispersion curve of the region with 300 defects per 1000 nm^2 is shifted to lower energies (by about 100 meV) with respect to that for a region with 100 defects per 1000 nm^2, consistent with our discussions above.

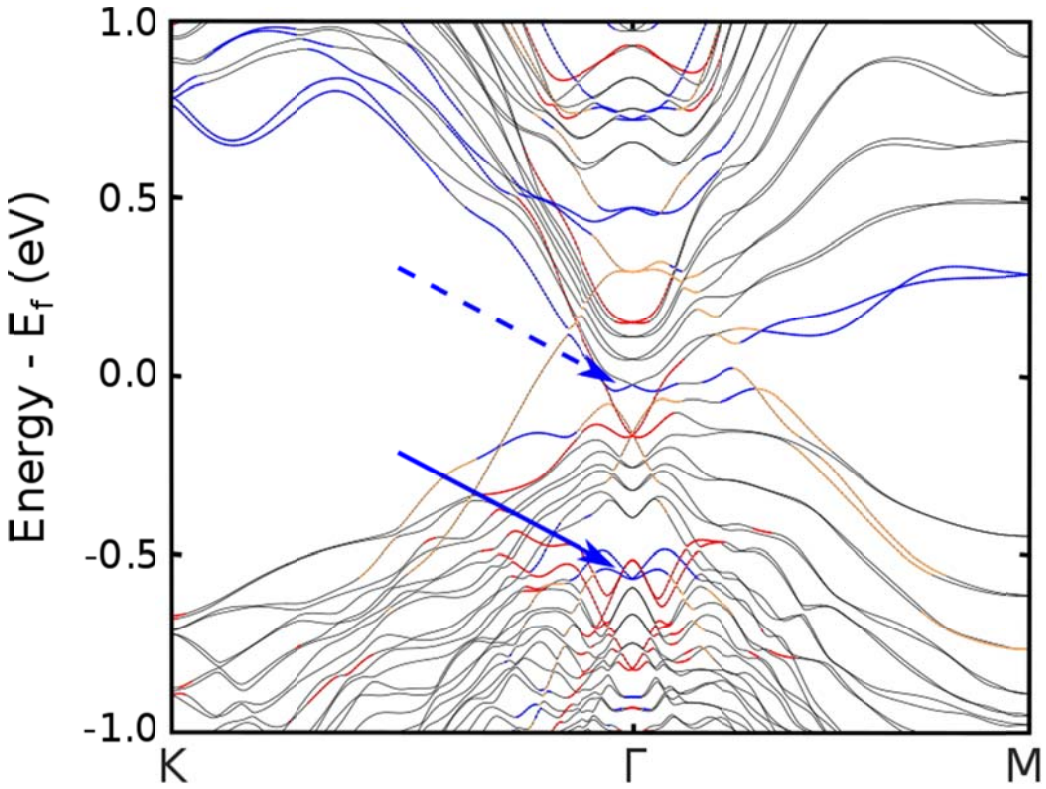

Figure SM-10: DFT-calculated band structure of the Bi-bilayer adsorbed on Bi_2Te_3. The Fermi level has been chosen as the zero of energy. The Bi bilayer is positioned on top of 5 QLs of Bi_2Te_3. The blue and red colors in the band structure indicate that most of the electron density corresponding with this level comes from the topmost or bottommost QL, respectively. The yellow color indicates the levels mainly located in the Bi bilayer. Due to the charge transfer from the Bi bilayer towards Bi_2Te_3, the original surface Dirac cone has shifted downwards (its binding energy has increased). This original Dirac cone is indicated by the full blue arrow. A new 'second' cone has appeared around the Fermi level, indicated by the dotted blue arrow. It originates from the lowest conduction band state of pristine Bi_2Te_3. This mechanism is similar to what was observed for the adsorption of a Bi bilayer on top of Bi_2Se_3 in Ref. [11].

References

(1) Sessi, P.; Otrokov, M. M.; Bathon, T.; Vergniory, M. G.; Tsirkin, S. S.; Kokh, K. A.; Tereshchenko, O. E.; Chulkov, E. V.; Bode, M. Visualizing Spin-Dependent Bulk Scattering and Breakdown of the Linear Dispersion Relation in Bi_2Te_3. *Phys. Rev. B* **2013,** 88, 161407(R).

(2) Sessi, P.; Bathon, T.; Kokh, K. A.; Tereshchenko, O. E.; Bode, M. Probing the Electronic Properties of Individual MnPc Molecules Coupled to Topological States. *Nano Lett.* **2014,** 14, 5092−5096.

(3) Alpichshev, Z.; Analytis, J. G.; Chu, J.-H.; Fisher, I. R.; Chen, Y. L.; Shen, Z. X.; Fang, A.; Kapitulnik, A. STM Imaging of Electronic Waves on the Surface of Bi_2Te_3: Topologically Protected Surface States and Hexagonal Warping Effects. *Phys. Rev. Lett.* **2010,** 104, 016401.

(4) Chen, T.; Chen, Q.; Schouteden, K.; Huang, W.; Wang, X.; Li, Z.; Miao, F.; Wang, X.; Li, Z.; Zhao, B.; Li, S.; Song, F.; Wang, J.; Wang, B.; Van Haesendonck, C.; Wang, G. Topological Transport and Atomic Tunneling-Clustering Dynamics for Aged Cu-Doped Bi_2Te_3 Crystals. *Nat. Commun.* **2014,** 5, 5022.

(5) Guo, Q.; Yin, F.; Palmer, R. E. Beyond the Herringbone Reconstruction: Magic Gold Fingers. *Small* **2005,** 1, 76.

(6) Teweldebrhan, D.; Goyal, V.; Balandin, A. A. Exfoliation and Characterization of Bismuth Telluride Atomic Quintuples and Quasi-Two-Dimensional Crystals. *Nano Lett.* **2010,** 10, 12010-1218.

(7) Steiner, H.; Volobuev, V.; Caha, O.; Bauer, G.; Springholz, G.; Holý, V. Structure and Composition of Bismuth Telluride Topological Insulators Grown by Molecular Beam Epitaxy. *J. Appl. Crystallogr.* **2014,** 47, 1889–1900.

(8) Yao, M.-Y.; Zhu, F.; Han, C. Q.; Guan, D. D.; Liu, C.; Qian, D.; Jia, J. Topologically Nontrivial Bismuth(111) Thin Films. *Sci. Rep.* **2016,** 6, 21326.

(9) Horcas, I.; Fernández, R.; Gómez-Rodríguez, J. M.; Colchero, J.; Gómez-Herrero, J.; Baro, A. M. WSxM: A Software for Scanning Probe Microscopy and a Tool for Nanotechnology. *Rev. Sci. Instrum.* **2007,** 78, 013705.

(10) Zhang, T.; Cheng, P.; Chen, X.; Jia, J.-F.; Ma, X.; He, K.; Wang, L.; Zhang, H.; Dai, X.; Fang, Z.; Xie, X.; Xue, Q.-K. Experimental Demonstration of Topological Surface States Protected by Time-Reversal Symmetry. *Phys. Rev. Lett.* **2009,** 103, 266803.

(11) Govaerts, K.; Park, K.; De Beule, C.; Partoens, B.; Lamoen, D. The Effect of Bi Bilayers on the Topological States of Bi_2Se_3: a First-Principles Study. *Phys. Rev. B* **2014,** 90, 155124.